JOURNAL OF PROPULSION AND POWER
Vol. 19, No. 4, July–August 2003

Improved Aerodynamic-Ramp Injector in Supersonic Flow

L. S. Jacobsen,* S. D. Gallimore,† J. A. Schetz,‡ and W. F. O'Brien§
Virginia Polytechnic Institute and State University, Blacksburg, Virginia 24061
and
L. P. Goss¶
Innovative Scientific Solutions, Inc., Dayton, Ohio 45440

An experimental study was performed in the Virginia Polytechnic Institute and State University supersonic wind tunnel on a simplified and revised multiport aerodynamic-ramp injector array in a supersonic flow. The new aerodynamic-ramp injector consisted of four flush-walled holes, in contrast to the original nine-hole versions. For comparison, a single, low downstream-angled circular injector hole was examined. Test conditions included sonic air injection into a Mach 2.4 air cross stream with an average Reynolds number of 4.2×10^7/m at jet-to-freestream momentum flux ratios from 1.1 to 3.3. Shadowgraphs and surface oil-flow visualization pictures were taken in the vicinity of the injectors to gain a qualitative assessment of the injector flowfields. Quantitative measurements of the pressure field on the surface near injectors and in a cross-stream plane downstream were conducted using pressure-sensitive paint and pitot/cone-static probes, respectively. The mixing characteristics of the injectors at three downstream stations were quantified using total temperature probes and a combination of heated and unheated injected air profiles to generate a mixing analog to concentration. Results showed that the aerodynamic-ramp mixed faster and had a larger plume area than the single-hole injector, while sustaining somewhat higher pressure losses due to increased blockage and a higher downstream-angled injector arrangement.

Nomenclature

A	=	cross-sectional area
C_d	=	discharge coefficient
d_{eq}	=	equivalent jet diameter, $d_j\sqrt{4}$ for a four-hole array
d_j	=	jet diameter
h_{mix}	=	maximum concentration penetration height
h_s	=	stoichiometric plume penetration height
l	=	injector throat length
$\dot{m}_{j,a}$	=	actual injector mass flux, $C_d\dot{m}_{j,i}$
$\dot{m}_{j,i}$	=	ideal injector mass flux
p	=	static pressure
p_t	=	total pressure
$\bar{q}$	=	jet-to-freestream momentum flux ratio
R_b	=	effective radius
Re	=	Reynolds number
T	=	static temperature
T_t	=	total temperature
u	=	flow speed
w_{core}	=	plume core width
w_{edge}	=	stoichiometric plume width
x	=	streamwise coordinate
y	=	spanwise coordinate
z	=	vertical coordinate
α_{mix}	=	mass fraction mixing analogy
$\alpha_{mix,max}$	=	maximum mixing analogy mass fraction
α_s	=	C_2H_4–air stoichiometric mass fraction, 0.068
γ	=	specific heat ratio
η_m	=	mixing efficiency
λ	=	jet-to-freestream mass flux ratio $(\rho u)_j/(\rho u)_\infty$
ρ	=	density

Subscripts

C	=	ambient injection temperature condition, cold injection
H	=	heated injection temperature condition, hot injection
j	=	injector
∞	=	freestream

Presented as Paper 2001-0518 at the AIAA 39th Aerospace Sciences Meeting, Reno, NV, 8–10 January 2001; received 10 October 2001; revision received 25 March 2003; accepted for publication 31 March 2003.

*Graduate Research Assistant, Department of Aerospace and Ocean Engineering; currently NRC Research Associate, Aerospace Propulsion Office, U.S. Air Force Research Laboratory, Wright–Patterson Air Force Base, OH 45433. Member AIAA.

†Graduate Research Assistant, Department of Mechanical Engineering; currently Aerospace Research Engineer, Hypersonic Airbreathing Propulsion Branch, Swales Aerospace, Langley, VA 23681. Member AIAA.

‡Fred D. Durham Chair, Department of Aerospace and Ocean Engineering. Fellow AIAA.

§Department Head, J. Bernard Jones Professor, Department of Mechanical Engineering. Associate Fellow AIAA.

¶President. Member AIAA.

Introduction

In a scramjet engine, not only must the injected fuel mix quickly into the surrounding freestream, the process must also induce the lowest aerothermodynamic losses possible because of short fuel residence times inside scramjet combustors on the order of a millisecond. Enhanced mixing and rapid combustion imply a reduction of the combustor length, thus, reducing the skin-friction drag and increasing the potential for positive net thrust. Higher total pressure losses lead to higher static temperatures in the combustor and, ultimately, a decrease in cycle efficiency.

A multitude of experiments have been performed in the field of injection in supersonic flows using numerous techniques, such as swept ramps,[1–3] slots,[4,5] transverse injection,[1,6–11] and jet swirl.[12–17] An extensive review of injector mixing characteristics is given by Schetz et al.[18]

The general interference effects generated by multihole transverse injector arrays have been capitalized on in the design of the "aero-ramp" injector by Cox et al.,[19] Cox-Stouffer and Gruber,[20–22] Fuller et al.,[23] and Schetz et al.[24] This design showed promising features, such as mixing characteristics near the same performance level of a physical ramp injector with lower total pressure losses. However, the design left a secondary core trapped in the shear layer near the wall, which could lead to undesirably high heat transfer rates along the combustor surface. The effects of toe-in angle on a single row injector array have also been examined by Jacobsen et al.[25] In that study, it was found that increasing the toe-in angle of the exterior injector holes greatly increased the mixing efficiency

and core penetration of the overall jet plume generated by the array. An attempt to capitalize on the effects of an aero-ramp injector array in a scramjet combustor were first numerically studied by Eklund and Gruber,[26] and then experimentally by Gruber et al.[27] In the latter study, two hydrocarbon-fueled aero-ramps were compared to a single row of four 15-deg low downstream-angled holes. Currently, the design and development of the aero-ramp injector involves the need for simplification of the difficult to fabricate, nine-hole design. A new simplified aero-ramp would use its configuration to enhance axial mixing and leave little to no fuel on the surface downstream of the injector. Future development of the aero-ramp should also include the possibility of incorporating a flame holding device somewhere in between, off center, or downstream of the fuel injector array.

Experiments were performed to investigate the flowfield near a new aerodynamic-ramp injector array. The new four-hole aero-ramp was designed to maximize axial jet-induced vorticity and to use this to lift the entire plume into the flow. The new aero-ramp injector was tested and compared to a single low-angled circular injector hole in a Mach 2.4 cross stream. Shadowgraph and surface flow visualization pictures were taken at momentum flux ratios from 1.1 to 3.3 to help qualitatively understand the nature of the flows. To assess the pressure losses incurred by the two injectors, pressure-sensitive paint and aerothermodynamic probing were used near the injector and at a downstream location, respectively. In addition, total temperature measurements were also taken at three downstream locations with heated air injection to help quantify the mixing capability of the injector array and compare it to the single-hole injector.

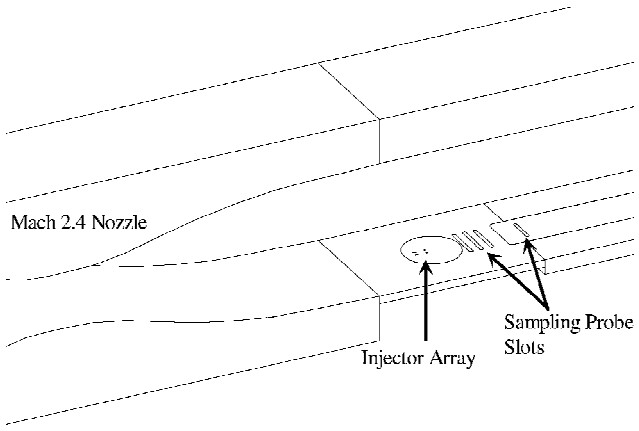

Fig. 1 Virginia Polytechnic Institute and State University Mach 2.4 test section, 23 × 23 × 30 cm.

Test Facilities

Experiments took place in the Virginia Polytechnic Institute and State University blowdown supersonic wind tunnel. The wind tunnel was configured with a convergent–divergent nozzle resulting in a freestream Mach number of 2.4. The test section dimensions were 23 cm wide by 23 cm high and 30 cm long in the streamwise direction. Data were acquired on a personal computer, a 16-channel, 16-bit A/D converter, and a 64-channel multiplexer with a built-in cold-junction compensator for temperature measurement. Figure 1 shows the wind tunnel nozzle and test section.

Injector Models

Figure 2 shows the two injector models used in this study. The aero-ramp injector used in the experiments had four jets, each with an individual jet diameter d_j of 2.38 mm and, therefore, an equivalent jet diameter d_{eq} of 4.76 mm. The design consisted of two rows of two round holes, spaced 4.0 equivalent jet diameters apart in the streamwise direction with a cross-stream spacing of 2.0 equivalent jet diameters between the holes. The first and second pair of injector holes had transverse-injection and toe-in angles of 20 and 40 deg and 15 and 30 deg, respectively.

Several candidate reference injectors were considered for comparison to the aero-ramp; of these, the most favorable choices were a swept ramp and a single-hole injector, downstream angled at either 15 deg or the equivalent composite angle of the injector array (~30 deg). Because the aero-ramp injector was being designed for combustion experiments in comparison to the baseline injector configuration from Gruber et al.,[27] which consisted of four, 15-deg low downstream-angled holes, a single hole from this arrangement was chosen. The single low-angled circular injector hole had a diameter of 5.61 mm and was transversely angled 15 deg relative to the downstream direction on the test section floor (Fig. 2b). The single-hole injector had a throat length of 6.0 l/d_j (measured from the center of the hole).

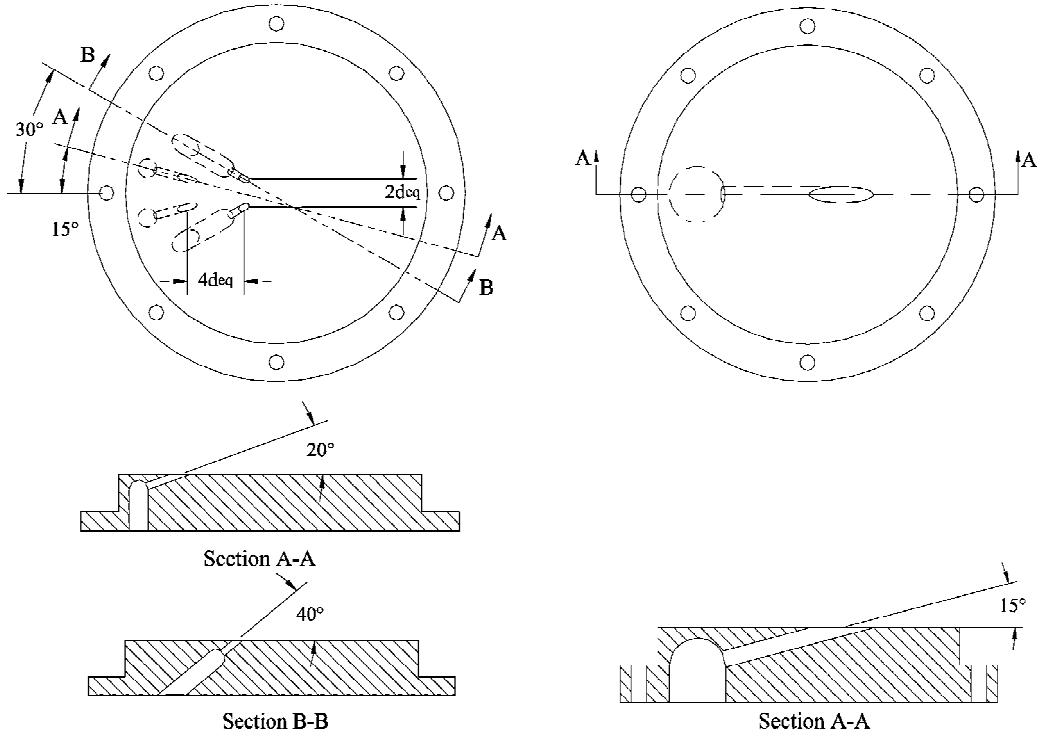

a) Aero-ramp injector array **b) Low-transverse-angled circular injector hole**

Fig. 2 Injector models.

Some of the main issues associated with the evolving design of the aero-ramp injector are the mitigation of a secondary fuel-core trapped in the shear layer near the surface, ways to generate vorticity and enhance mixing with the arrangement of the holes, and the possible accommodation of a spark, pilot, or plasma igniter downstream of the injector array. The current four-hole aero-ramp design is a simplification of the nine-hole version.[19–24] By the removal of the center row of holes in the nine-hole array and the inclusion of high toe-in angles of the existing holes, the current design encourages axial vortex formation. This helps to lift the entire plume off of the wall, leaving little to no secondary fuel core near the surface. This mitigation of the secondary core in the shear layer will help reduce the thermal loading to the surface of the combustor. Further simplification of the aero-ramp design involves the removal of one of the cross-stream rows of holes from the original nine-hole design as well. The angular placement and arrangement of the four-hole aero-ramp was designed to create a lean channel in between the two downstream rows of jets. The jet arrangement was also created to produce a sheltered region downstream, where flame ignition and propagation would be enhanced.

It is important to realize that the four-hole aerodynamic-ramp injector was designed by the study of parametric trends associated with the toe-in angle and swirl,[12,25] along with various other nine-hole aero-ramp studies, mainly involving computational fluid dynamics (CFD).[19–24] The new four-hole injector model is not formally optimized, however many of the features were selected to enhance its performance based on results from the similar studies listed above.

Test Matrix

All wind tunnel tests were performed at a freestream Mach number of 2.4 while injecting ambient or heated air to simulate hydrocarbon fuels without the associated safety hazard. The average total pressure and temperature of the freestream were 3.7 atm and 281 K, respectively. These conditions resulted in a corresponding freestream velocity of 550 m/s and a Reynolds number of 4.2×10^7/m. Tests involved jet-to-freestream momentum flux ratios ranging from 1.1 to 3.3. The jet-to-freestream momentum flux ratio is defined as

$$\bar{q} = \frac{(\rho u^2)_j}{(\rho u^2)_\infty} = \frac{(\gamma p M^2)_j}{(\gamma p M^2)_\infty} \tag{1}$$

Air from a supply tank was used as the injectant through the injector block and the momentum flux ratios were limited to a maximum value of 3.5. A throttling valve in the line allowed reduction to a nominal value of 1.1. Table 1 shows the matrix of test conditions examined in the experiments. Because the aero-ramp was designed to inject a set amount of gas at a higher jet-to-freestream momentum flux ratio than the single-hole injector, the experiments were segmented by set mass flux values for better comparison. Thus, for a given mass flow, the two injectors have an equivalent effective radius. The injector freestream flow coordinate system consists of right-hand Cartesian coordinates with the origin placed at the center of the overall injector areas. The positive x axis is in the downstream direction, the y axis in the horizontal direction, and the positive z axis in the vertical direction. The effective radius was used to normalize axial distance. The effective radius is defined as

$$R_b = \sqrt{\dot{m}_{j,a}/\rho_\infty u_\infty} \tag{2}$$

where $\dot{m}_{j,a}$ is the actual injector mass flux, equal to the ideal mass flux times the injector discharge coefficient $\dot{m}_{j,i} C_d$. The effective radius was originally defined by Barber et al.[9] as the radius of the equivalent circular area of freestream flow with a mass flux equal of that of the injectors except for a factor of π in the denominator.

Table 1 Nominal injector test conditions

	$\dot{m}_{j,i}$		
Injector	18 g/s	26 g/s	36 g/s
Aero-ramp	$\bar{q} = 1.5$	$\bar{q} = 2.2$	$\bar{q} = 3.0$
Single hole	$\bar{q} = 1.1$	——	$\bar{q} = 2.2$

The methodology for estimating the uncertainties in measurements and in the experimental results calculated from them, was based on the AIAA standard.[28] Estimation of the total uncertainty in the measured quantities utilized the precision index of the mean and bias error at a confidence level of 95% (20:1 odds). Uncertainty in the experimental results as a function of the measured variables was calculated using the Euclidean norm.

Apparatus and Techniques

Nanoshadowgraphs

Spark shadowgraphs were taken using a nanopulser spark with an exposure time of 2×10^{-8} s. With a 20-ns pulse of light, it is possible to see the turbulent eddy structures in the flow significantly larger than 0.011 mm.

Surface Oil-Flow Visualization

Visualization of the surface flow patterns near the injectors was accomplished via the use of 500-cSt silicone oil mixed separately with two colors of fluorescent dye. To help show the direction of the surface flow as it passed the injector holes, a thin layer of fluorescent green oil was placed all around the injector, and a thin strip of fluorescent red oil was placed in front of the injector holes. The patterns were illuminated with a 100-W ultraviolet lamp, and pictures were taken with a 35-mm camera after each run. The surface oil-flow patterns were also recorded on videotape during tunnel operation.

Aerothermodynamic Probing

Aerothermodynamic sampling was accomplished with pitot, cone-static, and total temperature probes. The pitot probe had a 1.59 mm outer diameter and 1.04 mm inner diameter, which gave a capture area of 0.85 mm^2. The cone-static probe consisted of 1.59-mm-outer-diameter pipe with a 10-deg cone half-angle. There were four small ports arranged around the cone to help reduce the effects of misalignment of the probe to the flow. Temperature was measured with a rake consisting of three 1.59-mm-outer-diameter tubes spaced 6.4 mm apart, each with a thermocouple inside. Each tube had an inner diameter of 1.04 mm, giving each probe a 0.85-mm^2 capture area. The total temperature probes also had four small holes drilled around the tubes to improve the recovery factors of the probes. The capture to recovery area ratio was 5–1, resulting in a recovery factor of 0.98. Exposed junction type-E thermocouples with 0.25-mm-diam beads were placed inside the three total temperature probes.

Pressure-Sensitive Paint

Measurements of the static pressure fields around the injectors were made using pressure-sensitive paint (PSP). The PSP used was based on a fluoroacrylic copolymer binder and incorporated the fluorinated platinum porphyrin species, meso-Tetra–(pentafluorophenyl)porphine. The PSP was illuminated in the near-UV range with a light-emitting diode-based array. The wavelength of the resulting luminescence of the paint occurred in the 500–600 nm range and was imaged on a charge-coupled device camera. Because of oxygen quenching effects, the resulting intensity profile is inversely proportional to the static pressure field around the injector. Calculation of the local static pressure field was done using an in-situ method involving sample calibration information of intensity as a function of temperature and pressure and information from one of the pressure taps on the surface near the injector. A detailed description of the PSP reduction process and theory is given by Crites.[29]

Species Composition Mixing Analogy

Aerothermodynamic sampling with the three total temperature probes attached to a rake mentioned earlier were performed for the test conditions in Table 1 with ambient and heated air as the injectant. This was done to obtain temperature profiles analogous to the mass fraction of a simulated hydrocarbon gas with a molecular weight similar to air, such as ethylene. During the heated runs, the air in the injector plenum chamber was raised approximately 60°C. The

mass fraction mixing analogy α_{mix} originally defined by Tomioka et al.,[6,30] is

$$\alpha_{\text{mix}} = \left(\left. \frac{T_t}{T_{t,\infty}} \right|_H - \left. \frac{T_t}{T_{t,\infty}} \right|_C \right) \Bigg/ \left[\left(\left. \frac{T_t}{T_{t,\infty}} \right|_H - \left. \frac{T_t}{T_{t,\infty}} \right|_C \right) - \left(\left. \frac{T_t}{T_{t,\infty}} \right|_H \left. \frac{T_{t,j}}{T_{t,\infty}} \right|_C - \left. \frac{T_t}{T_{t,\infty}} \right|_C \left. \frac{T_{t,j}}{T_{t,\infty}} \right|_H \right) \right] \tag{3}$$

where $T_{t,j}$ is the total temperature of the injected air and $T_{t,\infty}$ is the total temperature of the freestream flow. Note that the mixing analogy can also be derived in the same fashion for a flowfield with two different gases. The air in the injector plenum chamber was preheated using two 2000-W cartridge heaters inside a heating tank before entering the individual lines to the injector holes. In an effort to minimize the nonuniformity of temperature through each injector hole due to heat transfer, the outside walls of the copper injector lines were insulated and preheated by running hot air through the lines before the experiments.

Results and Analysis

To document the aero-ramp injector performance characteristics, experiments were performed on the new, four-hole, aero-ramp injector to obtain a more complete understanding of its flowfield. The results were compared to a single, sonic 15-deg downstream-angled hole. To make the comparison more direct in terms of a similar scramjet combustor configuration, the two injectors were compared on an equivalent mass flow basis. Thus, the aero-ramp was scaled up to an equivalent diameter of 4.76 mm for comparison to a full-scale 5.61-mm single 15-deg downstream-angled hole to operate in a range thought favorable to aero-ramp-type injectors. This placed the operating momentum flux ratio range of the aero-ramp at $1.1 \leq \bar{q} \leq 3.5$ for an equivalent injector mass flow comparison to the single-hole injector at $0.8 \leq \bar{q} \leq 2.5$, for the baseline configuration of Gruber et al.[27] Shadowgraph and surface-flow visualization pictures were taken at various momentum flux ratios to help qualitatively understand the nature of the flows. PSP and aerothermodynamic probing studies were made to assess the pressure losses incurred by the two injectors. In addition, total temperature measurements were taken at three downstream locations with heated air injection to help quantify the mixing capability of the injector array and to compare it to the single-hole injector.

Shadowgraphs

Shadowgraphs of the aerodynamic ramp and single-hole injectors in a Mach 2.4 crossflow are shown in Fig. 3. In all of the shadowgraphs, excluding the ambient injection cases, the flow is from left to right.

In the ambient environment pictures, the aero-ramp jets (Fig. 3a) are underexpanded 5.2 times, and a clear image of the expanding jets shock structures can be seen, including the barrel shocks, Mach disks, and shock trails. The ambient injection picture of the 3.5 times underexpanded, single-hole jet has roughly a 9% lower mass flow level than that of the aero-ramp picture. In Fig. 3b, less of the shock structures can be seen because the gas is less overexpanded than the aero-ramp, although a shock wave is evident emanating off the trailing edge of the injector hole. In these images, the relative injection angles of the injector plumes are also visible. The aero-ramp plume injection angle is about twice the relative transverse angle of that of the single-hole plume. This is due to the physical transverse injection angles of the two injectors (aero-ramp $\approx$ 30 deg and single hole = 15 deg).

In the supersonic crossflow pictures (Figs. 3c–3f), air is being injected through the aero-ramp injector at ideal mass flow values of 18 and 36 g/s, corresponding to jet-to-freestream momentum flux ratios $\bar{q}$ of 1.4 and 3.3 and through the single-hole injectors at 1.0 and 2.3, respectively. The lower and higher momentum flux ratios correspond to the same mass flow levels through the two injectors, and any discrepancy to the idealized momentum flux ratio values is due to variation of the freestream conditions on a run-to-run basis. The boundary layer near the injector is about 9 mm thick, and the bow shock waves produced from the two rows of injector holes in the injector array can be seen emanating from them, going up to the right. The shock structures of the injector jet plumes (Figs. 3c–3f) are masked by the turbulent structures in the boundary layer and are only partially visible. Still, it is possible to see how the plumes are turned downstream by the crossflow. The effect is especially visible in Figs. 3e and 3f. Because of the relatively small change in density associated with air injection into an air freestream and the thick boundary layer on the test section floor, the edge of the injector jet plumes downstream of the injection sites are slightly visible. Nevertheless, it is possible to see the injected air in the vicinity of the two injectors, but any estimate of the penetration height of the injected air would be purely speculative. The bow-shock-wave structures, which are readily seen emanating from above the injector jet plumes in the supersonic region of the boundary layer, are oblique and approach the angle of a Mach wave as they move away from the initial jet disturbances. The oblique bow shock waves produced from the injectors grow in strength (oblique angle) with the increase in momentum flux ratio $\bar{q}$. This means that the total-pressure losses incurred by the injection process may increase with $\bar{q}$ and corresponding mass flux due to increased blockage effects. The separation zones are distorted too much by the boundary layer and the unsteadiness of the injector to draw any conclusions about size or growth.

In the aero-ramp injector shadowgraphs (Figs. 3c and 3e) kinks in the bow shock can be seen emanating from the downstream row of injector jets. The kinks show the inherent unsteadiness created by the interactions of the jet plumes. Upstream of the injector, at the top left of the pictures, are other extraneous weak waves, which were created at the junction of the test section plate and the converging–diverging nozzle. In the aero-ramp images, a third, weaker shock wave created by the injection process can also be seen behind the two initial injector bow shocks. This shock wave is even more unsteady than the second bow shock and is the first shock in a trail of recompression shocks, created by the injector. The shock trail is especially evident in the surface flow visualization pictures (Fig. 4) and PSP images (Fig. 5) shown in the next two sections.

Surface Oil Flow

Figure 4 shows the results of the surface-oil-flow-visualization experiments. The pictures were taken at ideal mass flow values of 18 and 36 g/s, corresponding to injector jet-to-freestream momentum flux ratios $\bar{q}$ of 1.5 and 3.2 for the aero-ramp and 1.1 and 2.3 for the single-hole injector, respectively. Surface-oil-flow visualization gives a good indication of the flow around the two injectors. In all of the top-view surface-flow pictures (Fig. 4), the freestream flow was from left to right. Note that the actual pictures were taken from an angle off perpendicular, and a perspective change was made to view the images as from above. The exits of the injectors can be seen as elliptical black holes near the left edge. Just downstream of the aero-ramp injector, a slot can be seen. The slot was sealed with epoxy and sanded smooth to mitigate its effect on the surface flow-visualization experiments. The unstarting of the tunnel at the end of each run can sometimes have a distorting effect by pushing the paint on the surface in all directions. Although the unstart causes some distortion in the images, the surface-flow pictures still accurately represent the patterns created from the air injection as determined by video and direct observations during the runs.

A close inspection of the individual images can tell much about the various features involved in the flow patterns created by the injectors. Some of the important features are the trajectory of the jet plumes along the wall, the width of the individual jets and overall plumes, the size of the separation zones in front of the injector holes, and the separation regions behind the hole trailing edges.

The plume width is not apparent in these pictures (Fig. 4), because it is affected by the interaction of the toe-in angle of the injector and the freestream flow, which acts to lift the plume off the test section floor. The overlapping of the plumes due to the high toe-in angles of the aero-ramp injector indicates increased mixing between the individual injector jets. It was found in a similar study by Jacobsen et al.[25] that, as the jet momentum is angled in toward the center of

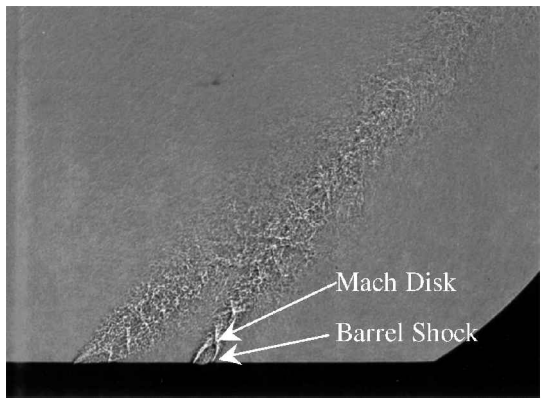

a) Aero-ramp, ambient jet, 5.2 times underexpanded, $\bar{q} = \infty$

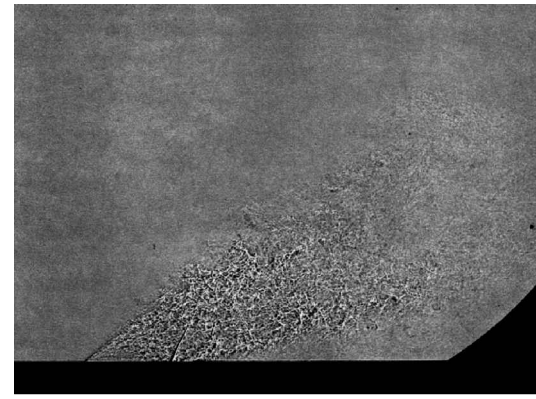

b) Single hole, ambient jet, 3.5 times underexpanded, $\bar{q} = \infty$

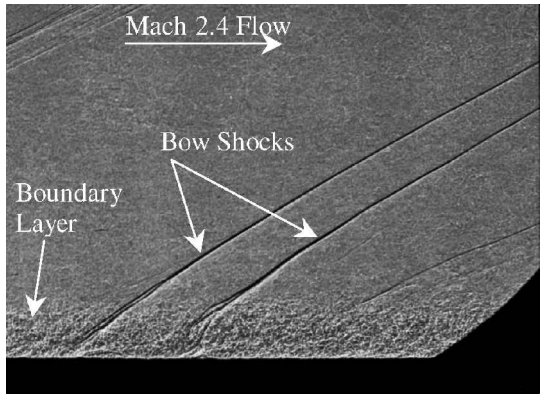

c) Aero-ramp, $\bar{q} = 1.4$, $\dot{m}_{j,i} = 18$ g/s

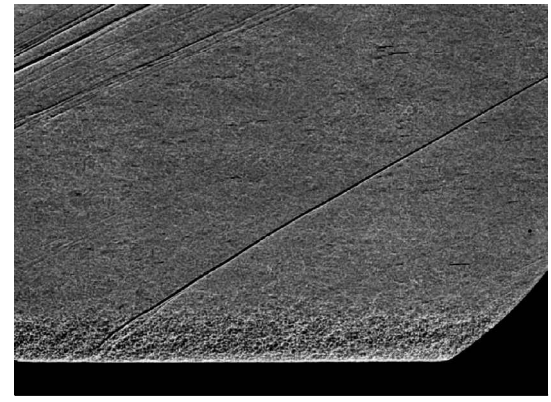

d) Single hole, $\bar{q} = 1.0$, $\dot{m}_{j,i} = 18$ g/s

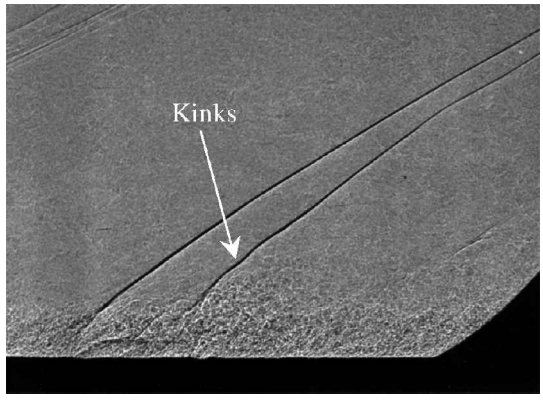

e) Aero-ramp, $\bar{q} = 3.3$, $\dot{m}_{j,i} = 36$ g/s

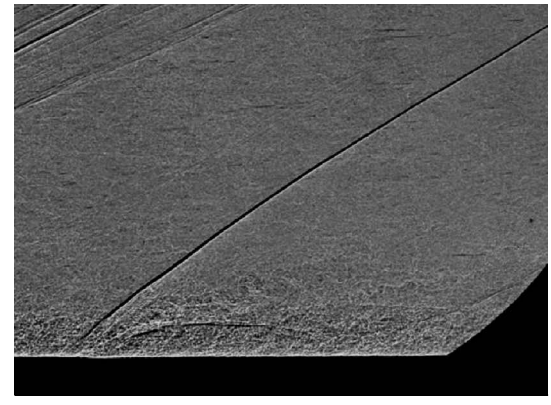

f) Single hole, $\bar{q} = 2.3$, $\dot{m}_{j,i} = 36$ g/s

Fig. 3 Shadowgraph images of the two injectors in an ambient environment and a Mach 2.4 crossflow.

an injector array, the penetration height of the injectant increased. Furthermore, as the jets expand inward, they reduce the width of the overall shock and confine the blockage to a narrower cross-stream space with a higher overall plume penetration.

The separation zones in front of the aero-ramp injector holes can be seen especially in the higher momentum flux ratio picture (Fig. 4c). In the cases with lower momentum flux ratios, the buildup of oil in this zone is seen to leak through between the first row of injector holes. As the momentum flux ratio increases, the surface flow through this region is reduced and finally stopped in the $\bar{q} = 3.2$ case. This separation zone is also seen in the higher $\bar{q}$ shadowgraph picture (Fig. 3e) and in the surface flow-video footage, which clearly shows the unsteady nature of this flow. The separation zone helps the jet plume initially penetrate farther by reducing the influence of the freestream momentum on that of the jets. However, such separations may create unwanted "hot spots" on the wall of a real combustor. The third separation zone can be seen directly behind the rear injector holes by the buildup of oil in this region. The zone increases in size with momentum flux ratio. Examination of the video footage shows the paint spinning and jumping around in the middle and downstream separation regions during tunnel operation, clearly indicating that the injector creates strong vortices that terminate on the wall. The downstream separation zone should provide a sheltered region good for ignition and flame propagation purposes. The size of the separation zones in front of and behind the single-hole injector are a lot smaller, and no conclusive trend was evident pertaining to their growth in size with momentum flux ratio/mass flow from the two pictures presented (Figs. 4b and 4e). However, it is clear that they are significantly smaller than the ones created by the aero-ramp array. Furthermore, note, in the low $\bar{q} = 1.1$ case (Fig. 4b), that oil flow can be seen to dip down into the recess of the single hole at its downstream end. This shows that the jet flow has effectively unattached itself from the contour of the hole, expanding at an increased transverse jet angle.

PSP

Experiments using PSP were conducted on the two injectors for ideal mass flow values of 18 and 36 g/s, corresponding nominally to

a) Aero-ramp, $\bar{q} = 1.5$, $\dot{m}_{j,i} = 18$ g/s

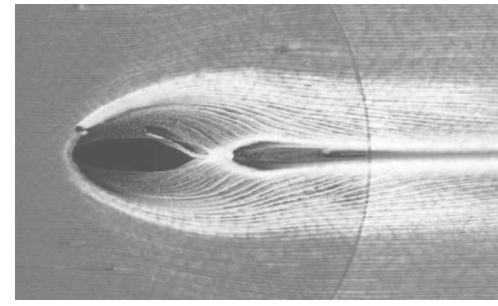

b) Single hole, $\bar{q} = 1.1$, $\dot{m}_{j,i} = 18$ g/s

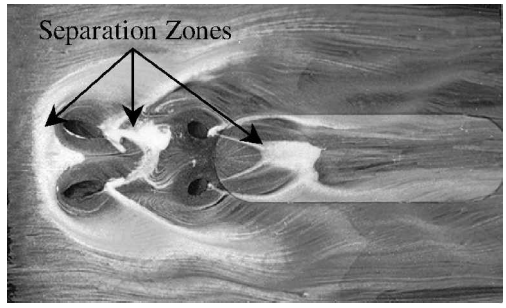

c) Aero-ramp, $\bar{q} = 3.2$, $\dot{m}_{j,i} = 36$ g/s

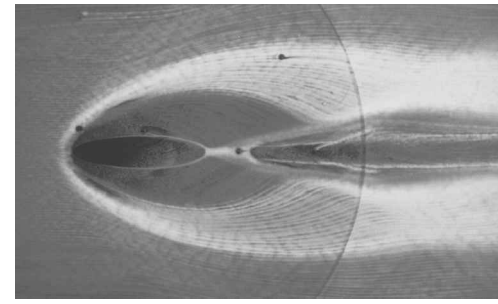

d) Single hole, $\bar{q} = 2.3$, $\dot{m}_{j,i} = 36$ g/s

Fig. 4 Surface oil-flow visualizations in a Mach 2.4 crossflow.

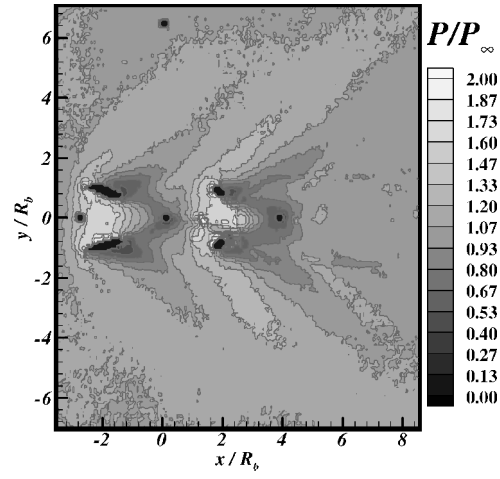

a) Aero-ramp, $\dot{m}_{j,i} = 18$ g/s, $\bar{q} = 1.5$

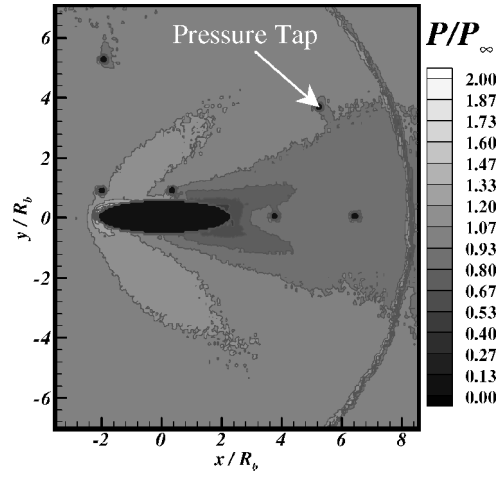

b) Single hole, $\dot{m}_{j,i} = 18$ g/s, $\bar{q} = 1.0$

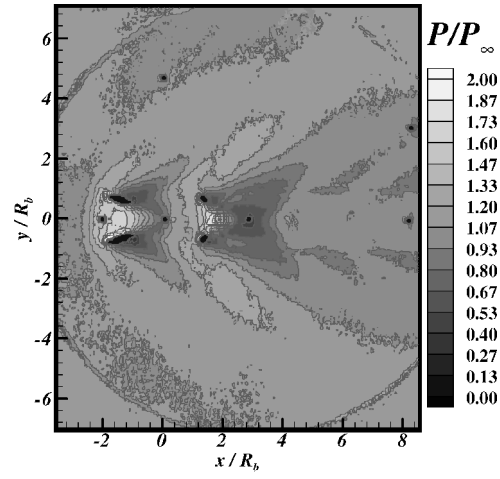

c) Aero-ramp, $\dot{m}_{j,i} = 36$ g/s, $\bar{q} = 2.8$

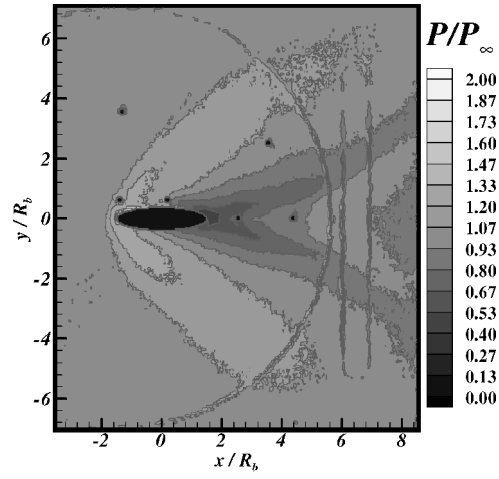

d) Single hole, $\dot{m}_{j,i} = 36$ g/s, $\bar{q} = 2.2$

Fig. 5 Normalized PSP experiments in a Mach 2.4 crossflow.

injector jet-to-freestream momentum flux ratios $\bar{q}$ of 1.5 and 2.8 for the aero-ramp and 1.0 and 2.2 for the single-hole injector, respectively. The results from this experiment, presented in Fig. 5, provide information about the static pressure field on the surface around the injector area. In Fig. 5, the flow is moving from left to right, and the pressure field is normalized by the freestream static pressure P_∞. Each plot of Fig. 5 has the same pressure scale to help with comparison. The surface x and y axes are shown normalized by the effective radius. While painting the injectors, the pressure tap holes and injector holes were plugged with small wires and tape, respectively. The thickness of the paint is only a few micrometers, and so no influence on the performance of the injector holes was expected. The dark circle around the injector area is where the surface of the tunnel mates with the injector blocks, and there is no paint. Because of a difference in temperature between the injector block and the test section wall, the pressure information outside of the circular injector block has a higher associated error. Additionally, the unsteady temperature variations associated with the blowdown facility caused the maximum deviation in calculated static pressure near the injector from the surface pressure taps to be 0.06 atm. This is because the pressure field was calculated using information from only a single pressure tap on the injector block in the downstream wake of the jet, which was used to estimate the entire injector-block temperature field. Hence, the maximum deviation of the static pressure calculated from the PSP field in the wake of the injector, relative to the surface pressure taps, is only 0.03 atm. The estimated uncertainty in the static pressure tap measurements was ± 0.004 atm. To illustrate this, two graphs of the centerline information of the surface pressure field compared to the centrally located pressure taps are shown as Fig. 6.

In the PSP pictures (Fig. 5), the high-pressure regions in front of the injector holes are caused by their corresponding bow shock waves. These high-pressure regions match up nicely to the separation zones shown in Fig. 4. Ultimately, these static surface pressure profiles show that the aero-ramp injector produced higher surface pressure over a larger area than the single-hole injector, indicating higher shock-related total-pressure losses from the injection process. The low-pressure regions behind the injector holes are the regions where the injector jets are expanding to reach the local surrounding backpressure. An interesting feature of the aero-ramp pressure profiles shown in Figs. 5a and 5c is the shock trail shown downstream of the injector. The shock trail is due to the underexpanded nature of the jet flowfield. Notably, this feature is not evident in the field of view of the single-hole images.

Aerothermodynamic Measurements: Total Pressure Profiles

Total pressure loss profiles of the aerodynamic-ramp injector are shown in Fig. 7. Figure 7 shows the results from the aerothermodynamic measurement experiments using pitot and cone-static probes. The measurements were made at sampling station 2, which normalized by the effective radius, corresponds to nondimensional distances of $6.0R_b$ and $6.3R_b$ from the centers of the aero-ramp and single-hole overall areas, respectively. The profiles were made at an ideal mass flux of 36 g/s corresponding to $\bar{q}$ of 3.0 ± 0.15 and 2.2 ± 0.11 with the aero-ramp and the single-hole injector, respectively. These isobar profiles (Fig. 7) illustrate the total pressure field produced by the injection process near the plumes of the injectors and allow a quantitative assessment of the losses incurred by the injectors. The local total pressure profiles are normalized by the freestream total pressure, and both profiles are set to the same non-dimensional scale for ease of comparison. The calculated uncertainty in $P_{t,\infty}$, $P_{t,j}$, and P_t were ± 0.07, ± 0.004, and ± 0.04 atm, respectively. The cross-stream isobar profile horizontal and vertical probe sampling locations were spaced 1.59 and 0.79 mm apart in the y and z direction over a distance of 50.8 and 30.5 mm, respectively. The uncertainty in probe position was ± 0.2 and ± 0.1 mm in the cross-stream and vertical positions, respectively.

In agreement with the PSP images, the total pressure loss profiles show the aero-ramp produced higher pressure losses in a larger area compared to the single-hole injector. In addition, the minimum pressure cores of the aero-ramp are lower and penetrate less into the freestream. The two outer-minimum total pressure cores are also spread farther apart in the aero-ramp configuration, which is directly due to the cross-stream injector spacing of the array. This implies that reducing the cross-stream spacing of the jets in the aero-ramp injector array will reduce the pressure losses by decreasing the total amount of freestream blockage. The total pressure losses are quantified in a later section.

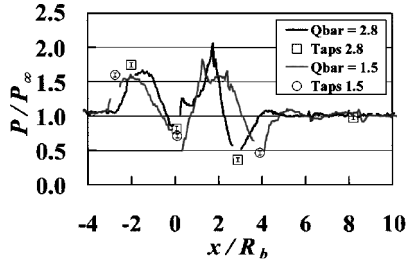

a) Aero-ramp injector

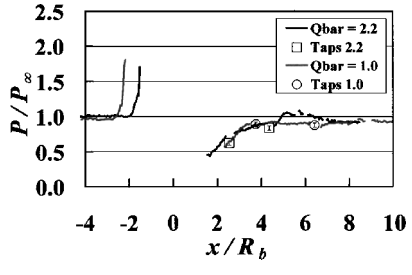

b) Single-hole injector

Fig. 6 Normalized PSP centerline traces.

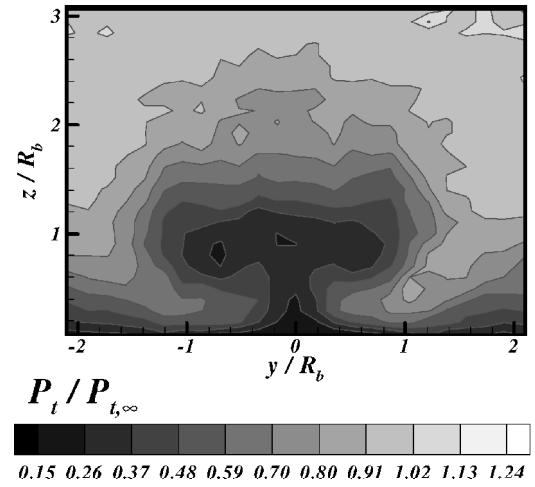

a) Aero-ramp injector, station 2, $\dot{m}_{j,i} = 36$ g/s, $\bar{q} = 3.0$, $x/R_b = 6.0$

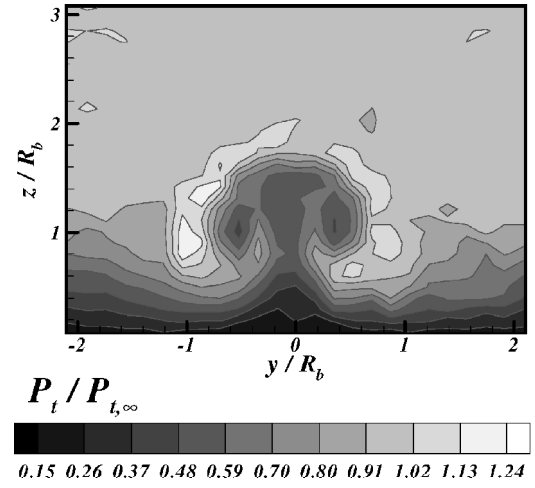

b) Single-hole injector, station 2, $\dot{m}_{j,i} = 36$ g/s, $\bar{q} = 2.2$, $x/R_b = 6.3$

Fig. 7 Downstream total pressure profiles.

Species Composition Mixing Analogy Profiles

The mixing analogy profiles created using Eq. (3) for the aero-ramp and single-hole injectors are presented in Figs. 8 and 9, respectively. The scale of the isoline mixing analogy profiles shown in both Figs. 8 and 9 are set the same from zero to the highest concentration level observed by the aero-ramp injector at the closest measurement station to the injector. The downstream distances of the cross-stream profiles are measured from the centers of the overall injector area and are normalized by the effective radius. Downstream mixing analogy concentration profiles were generated for all of the conditions listed in Table 1 with a maximum allowed run-to-run momentum flux ratio variation of ±5% in the profiles. The uncertainty in the measured temperatures used in deducing the mixing analogy was ±2 K. The calculated uncertainty in the mixing analogy α_{mix} from the measured quantities was ±0.03. The horizontal and vertical probe sampling locations were spaced apart in the same fashion as noted in the aerothermodynamic measurements from the preceding section. As already stated, the uncertainty in probe position was ±0.2 and ±0.1 mm in the cross-stream and vertical positions, respectively.

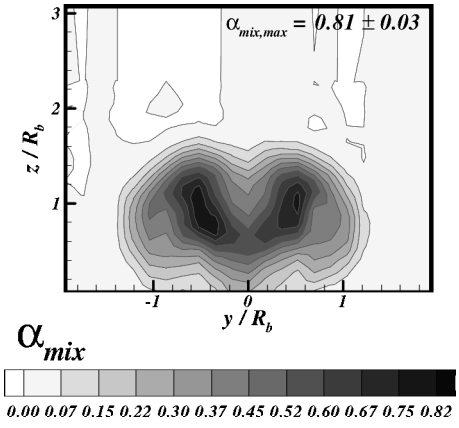

a) Station 1, $\dot{m}_{j,i}$ = 36 g/s, $\bar{q}$ = 3.0, x/R_b = 1.8

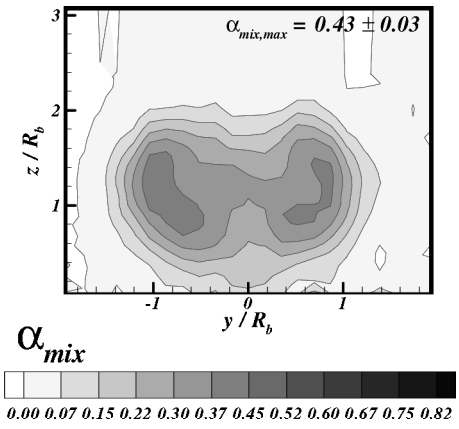

b) Station 2, $\dot{m}_{j,i}$ = 36 g/s, $\bar{q}$ = 3.0, x/R_b = 6.0

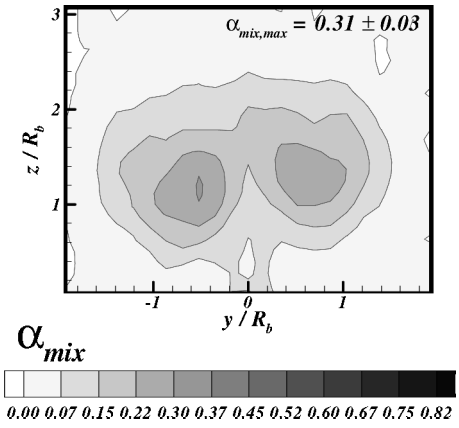

c) Station 3, $\dot{m}_{j,i}$ = 36 g/s, $\bar{q}$ = 3.0, x/R_b = 13.9

Fig. 8 Aero-ramp species composition mixing analogy profiles.

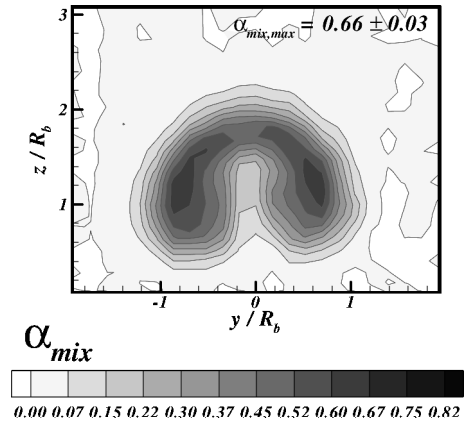

a) Station 2, $\dot{m}_{j,i}$ = 36 g/s, $\bar{q}$ = 2.2, x/R_b = 6.3

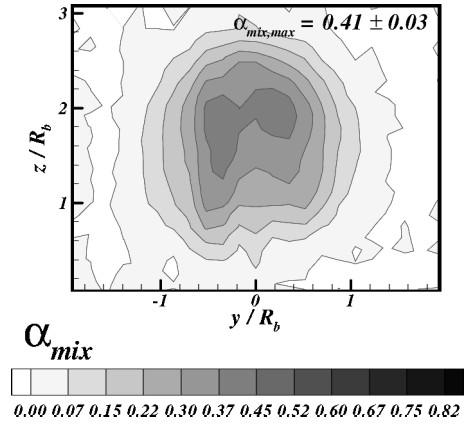

b) Station 3, $\dot{m}_{j,i}$ = 36 g/s, $\bar{q}$ = 2.2, x/R_b = 14.4

Fig. 9 Single-hole species composition mixing analogy profiles.

The aero-ramp mixing analogy profiles in Fig. 8 show that a significant single counter-rotating axial vortex structure has been created by the injector array, which is evident by the shape of the two primary injector cores. Furthermore, the injected air has been lifted away from the test section floor by the vortex motion, leaving no secondary core trapped on the surface by the shear layer. This is a significant difference from the earlier nine-hole aero-ramp injector plumes, which have been shown to trap a secondary core along the surface in the shear layer.[23] Figure 9 presents the mixing analogy profiles for the single-hole injector. For comparison to the aero-ramp, a limited number of profiles were obtained with the single-hole injector. The profiles show the aero-ramp to have a lower maximum mass fraction with a larger overall plume area and faster decay rate. These items will be quantified subsequently.

An interesting feature of the single-hole injector mixing analogy plumes is the horseshoe-shaped structure especially apparent in Fig. 9a. This shape is often associated with a vortex structure generated by the interaction of a jet in a crossflow and is the main mechanism for mixing enhancement of the single-hole jet. The aero-ramp, on the other hand, generates vorticity not only by freestream–jet interactions, but also from the interference effects of the multiple jet interactions and the toe-in of the jets, not to mention the additional vorticity generated by the multiple curved jet bow shocks.

Maximum Concentration Decay

The maximum concentration decay of the aero-ramp using the mixing analogy $\alpha_{\text{mix,max}}$ is shown in Fig. 10 and the vertical heights of the local core maximums, h_{mix}/R_b, are shown in Fig. 11. Figures 10 and 11 show that both injectors are better mixers at

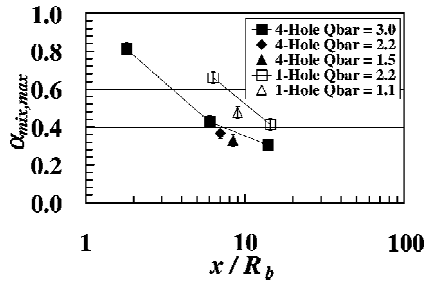

Fig. 10 Maximum analogous concentration decay.

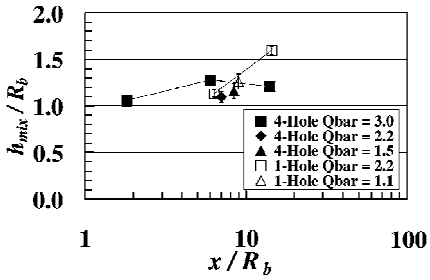

Fig. 11 Maximum analogous concentration core penetration height.

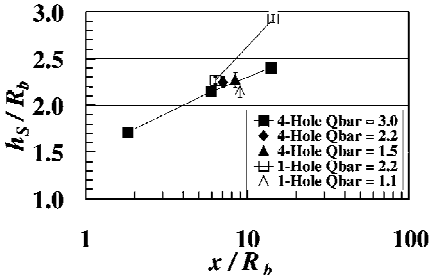

Fig. 12 Plume top penetration height.

lower momentum flux ratios and that the penetration heights of the plume cores are reduced. Overall, the aero-ramp provided better mixing in terms of lower maximum concentration at all comparable conditions tested. Another interesting trend shown in Fig. 11 is the high initial penetration height of the aero-ramp injector and how the single-hole core penetrates higher, farther downstream. This is partially due to the higher composite downstream angle of the aero-ramp array (≈ 30 deg) over that of the single-hole injector (15 deg). The higher transverse injection angle helps provide higher initial penetration; however, because of the spread out nature of the jets, the downstream penetration height is reduced, and the single-hole injector overtakes the aero-ramps plume.

Plume Penetration

The maximum penetration heights of the mixing analogy plumes, h_s/R_b, were measured, and the results are presented in Fig. 12. The plume penetration h_s is defined here as the vertical distance from the wall to the upper edge of the mixing region where the mass fraction mixing analogy is equal to the stoichiometric value of ethylene, 0.068. The results show the single-hole injector enables higher penetration at the higher momentum flux ratio and corresponding mass flow rate.

Plume Width

Figures 13 and 14 present the results from the plume width studies defined by the distance between the plume cores, w_{core}, and the stoichiometric side edges, w_{edge}, respectively. In the plume core width study, note that the cores start at an initial close relative position, move outward, and then return toward the centerline of the plumes. Also, as shown in Fig. 14, the width of the overall aero-ramp plume increases as a function of downstream distance, whereas the width

Table 2 Injector plume parameters for $x/R_b \approx 6$

Parameter	Aero-ramp	Single hole
A/A_u	6.4 ± 0.1	4.5 ± 0.1
η_m	0.30 ± 0.01	0.23 ± 0.01
Π	0.23 ± 0.05	0.21 ± 0.05

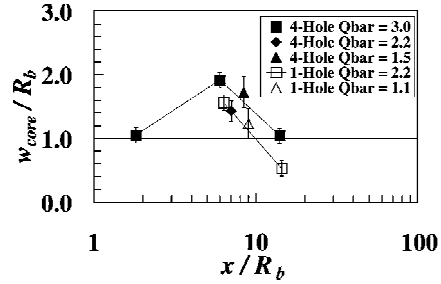

Fig. 13 Width between the plume cores.

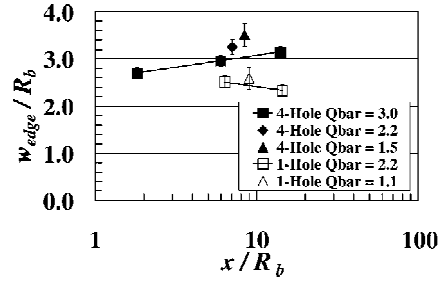

Fig. 14 Overall plume width.

from the single-holes decreases. This means that the aero-ramp produces a significant amount of lateral mixing.

Plume Area

The overall plume area is defined here as the total area of the plume that has an α_{mix} greater or equal to the stoichiometric value of ethylene, 0.068. Results from this study are presented in Table 2 for the data taken with an ideal mass flow level of 36 g/s at station 2, corresponding to $\bar{q}$ of 3.0 ± 0.15 and 2.2 ± 0.11 with the aero-ramp and the single-hole injector, respectively. The overstoichiometric plume areas are normalized by A_u, the area of an isentropically expanded jet with a static pressure equal to that of the freestream. The results show that the overstoichiometric plume area of the aero-ramp injector array is larger than that of the single-hole injector.

Mixing Efficiency

The mixing efficiency[31] is represented as "that fraction of the least available reactant which would react if the fuel–air mixture were brought to a chemical equilibrium without additional local or global mixing."[23] This means that the local fuel and air are considered mixed in the rich and lean fuel areas respectively. Here

$$\eta_m \equiv \frac{\dot{m}_{f,\text{mix}}}{\dot{m}_{f,\text{tot}}} = \frac{\int \alpha_r \rho u d A}{\int \alpha_{\text{mix}} \rho u d A} \tag{4}$$

where

$$\alpha_r \equiv \begin{cases} \alpha_{\text{mix}}, & \alpha_{\text{mix}} \le \alpha_s l \\ [(1-\alpha_{\text{mix}})/(1-\alpha_s)]\alpha_s, & \alpha_{\text{mix}} > \alpha_s \end{cases} \tag{5}$$

Table 2 presents the results for the sampling station $\sim 6R_b$ from the center of areas of the two injectors, which show that the mixing efficiency value of the aero-ramp injector model is higher than that for the single-hole injector model. The uncertainty in local velocity, Mach number, and density were ± 0.7 m/s, ± 0.03, and ± 0.004 kg/m^3.

Total Pressure Loss Parameter

The total pressure losses have been quantified using the total pressure loss parameter defined by Fuller et al.[23] This method simplifies the analysis by allowing an assessment of the losses within the sampling area. This total pressure loss parameter is defined as

$$\Pi = \frac{\int \rho u (p_{t,\infty} - p_t)\, \mathrm{d}A}{\rho_\infty u_\infty p_{t,\infty} A_s + \rho_j u_j p_{t,j} A_j} \tag{6}$$

where

$$A_s = (\lambda/\alpha_s) A_j \tag{7}$$

Thus, a fuel injector incurring no losses would have $\Pi = 0$. The results of the total pressure loss parameter for the sampling station $\sim 6R_b$ from the center of areas of the two injectors are presented in Table 2. These results show the single-hole injector to have only slightly lower total losses compared to the aero-ramp injector. At first glance, this may seem counterintuitive, due to the significantly lower "raw" total pressure losses shown in the total pressure profiles in Fig. 7. However, because the total pressure loss parameter is a mass-averaged quantity, the parameter is not assessed on pressure alone, but on density and velocity as well. It turns out that the plume of the single-hole injector has a higher velocity field near the jet plume. This high-velocity field significantly offsets the reduction in the total pressure loss parameter due to the lower total pressure losses because this would imply a higher mass flow in the sampling area.

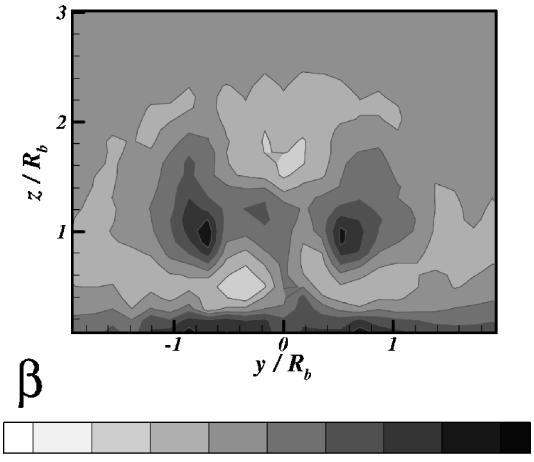

a) Aero-ramp injector, station 2, $\dot{m}_{j,i} = 36$ g/s, $\bar{q} = 3.0$, $x/R_b = 6.0$

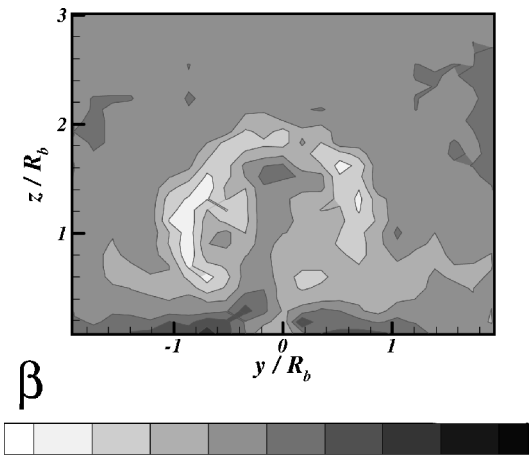

b) Single-hole injector, station 2, $\dot{m}_{j,i} = 36$ g/s, $\bar{q} = 2.2$, $x/R_b = 6.3$

Fig. 15 Enthalpy deficit factor due to vorticity.

Enthalpy Deficit Factor

The enthalpy deficit factor was originally defined by Tomioka et al.[6] by assuming a total enthalpy equation of the form

$$h_t = [h_{t,j}\alpha + h_{t,\infty}(1-\alpha)](1-\beta) \tag{8}$$

where α is the fuel mass fraction and β is the enthalpy deficit due to vorticity effects in the flowfield. When constant specific heats, air injection into an air freestream, and that α is equal to α_{mix} are assumed, the mass fraction distribution of the hot- and cold-air injection profiles are equal. Then one can write the following equation for β:

$$\beta = \frac{\alpha_{\text{mix}}(T_{t,j}/T_{t,\infty} - 1) - (T_t/T_{t,\infty} - 1)}{\alpha_{\text{mix}}(T_{t,j}/T_{t,\infty} - 1) + 1} \tag{9}$$

Figure 15 presents the results of using equation (9) for the total temperature and mixing analogy data at station 2 corresponding to a nominal distance of $x/R_b \approx 6$ downstream from the center of the injector areas, with an ideal mass flow level of 36 g/s, corresponding to $\bar{q}$ of 3.0 ± 0.15 and 2.2 ± 0.11 with the aero-ramp and the single-hole injector, respectively. For an uncertainty in the measured temperatures equal to ± 2 K and mixing analogy of ± 0.03, the calculated uncertainty in the enthalpy deficit factor was estimated to be ± 0.008. From Figs. 15, the locations of maximum total temperature change due to vorticity can be seen as the high and low β regions at and around the cores of the jets. Note that β cores in the aero-ramp injector profile shown in Fig. 15a are a lot higher than those for the single-hole injector in Fig. 15b, whereas the low β regions around the injector cores are lower in the single-hole injector profile. The high (+) and low (−) deficit factor regions correspond physically to regions of cooler and warmer total temperature relative to the freestream value, respectively.

Conclusions

Experiments were performed to investigate the flowfield near a new aero-ramp injector array. The new aero-ramp injector featured four holes, compared to the original nine-hole design, and was compared to a single, low-angled circular injector hole. Both injectors were exposed to a Mach 2.4 cross stream. Shadowgraph and surface-flow-visualization pictures were taken at various momentum flux ratios to help qualitatively understand the nature of the flows. PSP and aerothermodynamic probing were done to assess the pressure losses incurred by the two injectors. In addition, total temperature measurements were also taken at three downstream locations with heated air injection to help quantify the mixing capability incurred by the injector array and compare it to the single-hole injector.

The aero-ramp injector mixed better than the single-hole injector, as shown by the mixing efficiency values of 30 ± 1 and $23 \pm 1\%$ for the measurements made at nominally $6R_b$ downstream of the two fuel injectors. The decay rate was faster, and the level of the maximum mixing analogy concentration for the aero-ramp was lower than the single-hole injector at all stations measured. The plume of the aero-ramp had a larger plume area encompassing 42% more area at nominally $6R_b$ than the single-hole injector due to lateral spreading and faster mixing. This was due to the relatively large cross-stream distance between the individual injector holes. This large cross-stream distance also caused an overall reduction of the obtainable penetration height of the aero-ramp injector plume. In addition, the aero-ramp plume had a higher initial mixing analogy concentration core penetration height but was overtaken by the single-hole injector at the farthest downstream location tested.

The aero-ramp injector showed somewhat higher (10%) local total pressure losses than the single-hole injector. This was due to the higher composite angle injection of the aero-ramp array and the multiple shock structures from the two rows of jets. Although the local total pressure losses appeared more substantial, the mass-averaged total pressure loss parameter showed the aero-ramp to have only slightly higher overall losses.

The aero-ramp produced large separation zones in front, in between, and behind the injector jets. This would allow an increased

opportunity for flame holding in a high-enthalpy flow, but might also create hot spots on the surface near the injector. The cross spacing of the injector jets and the large separation zones create a sheltered channel, which could be capitalized on with some type of ignition aid such as a spark, pilot, or plasma-torch igniter. The relatively large area of mixed fuel and air between the aero-ramp plume cores, coupled with the low-velocity region behind the rear separation zone of the aero-ramp, could provide a suitable region for flame initiation and rapid spreading into the jet plume.

Further development of the design of the aero-ramp may include an array with lower downstream transverse injection angles, with a closer cross-stream spacing of the jets to reduce blockage. The size of the separation zones can also be reduced with a decrease of toe-in angle of the injector jets. This, however, may reduce mixing performance of the overall injection process. Disregarding the size of the separation zones, one may opt to increase the toe-in angle, which may offer increased mixing and penetration of the aero-ramp injector jet plume.

The high toe-in angles of the aero-ramps jets are thought to be the reason for the single, well-formed counter-rotating pair of jet vortices in the plume. This general behavior has been seen in the earlier toe-in studies, by Jacobsen et al.[25] The high toe-in angles of the four-hole array are also thought to increase the mixing efficiency of the main plume and to lift the plume off the wall. Increasing the mixing efficiency with toe-in though, should not be taken for granted just yet. It was found in earlier CFD studies,[21] with a nine-hole aero-ramp array with a smaller cross-stream spacing, that toe-in of the outer jets caused the array to mix slower than an array with no toe-in at all. This seems to be contradictory to the experimental data taken in the toe-in study of Jacobsen et al.[25] However, the mixing analogy as defined by Eq. (3) did not exist at the time of this study, and an earlier form was used that did not take into account the distortion of the concentration plume due to vorticity.

References

[1]Heiser, W. H., Pratt, D. T., Daley, D. H., and Mehta, U. B., "Hypersonic Airbreathing Propulsion," edited by J. S. Przemieniecki, AIAA Education Series, AIAA, Washington, DC, 1994, pp. 305–312.

[2]Hartfield, R. J., Hollo, S. D., and McDaniel, J. C., "Experimental Investigations of a Supersonic Swept Ramp Injector Using Laser Induced Iodine Fluorescence," *Journal of Propulsion and Power*, Vol. 10, No. 1, 1994, pp. 129–135.

[3]Riggins, D. W., and Vitt, P. H., "Vortex Generation and Mixing in Three-Dimensional Supersonic Combustors," *Journal of Propulsion and Power*, Vol. 11, No. 3, 1995, pp. 419–426.

[4]Lewis, D. P., and Schetz, J. A., "Tangential Injection from Overlaid Slots into a Supersonic Stream," *Journal of Propulsion and Power*, Vol. 13, No. 1, 1997, pp. 59–63.

[5]Schetz, J. A., Billig, F. S., Favin, S., and Gilreath, H. E., "Effects of Pressure Mismatch on Slot Injection in a Supersonic Flow," *International Journal of Turbo and Jet Engines*, Vol. 9, No. 2, 1992, pp. 135–146.

[6]Tomioka, S., Jacobsen, L. S., and Schetz, J. A., "Sonic Injection from Diamond-Shaped Orifices into a Supersonic Crossflow," *Journal of Propulsion and Power*, Vol. 19, No. 1, 2003, pp. 104–114.

[7]Schetz, J. A., "Interaction Shock Shape for Transverse Injection," *Journal of Spacecraft and Rockets*, Vol. 7, No. 2, 1970, pp. 143–149.

[8]Fuller, E. J., Mays, R. B., Thomas R. H., and Schetz, J. A., "Mixing Studies of Helium at High Supersonic Speeds," *AIAA Journal*, Vol. 30, No. 9, 1992, pp. 2234–2243.

[9]Barber, M. J., Roe, L. A., and Schetz, J. A., "Normal, Sonic Helium Injection Through a Wedge-Shaped Orifice in Supersonic Flow," *Journal of Propulsion and Power*, Vol. 13, No. 2, 1997, pp. 257–263.

[10]McClinton, C. R., "The Effect of Injection Angle on the interaction Between Sonic Secondary Jets and a Supersonic Freestream," NASA TND-6669, Feb. 1972.

[11]Rogers, R. C., "A Study of the Mixing of Hydrogen Injected Normal to a Supersonic Airstream," NASA TN L-7386, March 1971.

[12]Jacobsen, L. J., Schetz, J. A., Gallimore, S. D., and O'Brien, W. F., "Mixing Enhancement by Jet Swirl in a Multiport Injector Array in Supersonic Flow," *Proceedings of the 3rd ASME/JSME Joint Fluids Engineering Conference*, FEDSM99-7248, American Society of Mechanical Engineers, Fairfield, NJ, 1999.

[13]Kraus, D. K., and Cutler, A. D., "Mixing of Swirling Jets in a Supersonic Duct Flow," *Journal of Propulsion and Power*, Vol. 12, No. 1, 1996, pp. 170–177.

[14]Cutler, A. D., and Johnson C. H., "The Use of Swirling Jet Pairs to Provide Rapid Fuel Penetration in Scramjet Combustors," AIAA Paper 95-0099, Jan. 1995.

[15]Schetz, J. A., *Injection and Mixing in a Turbulent Flow*, AIAA, New York, 1980, Chap. 5, pp. 111–122.

[16]Povinelli, L. A., and Ehlers, R. C., "Swirling Base Injection for Supersonic Combustion Ramjets," *AIAA Journal*, Vol. 10, No. 9, 1972, pp. 1243–1244.

[17]Schetz, J. A., and Swanson R. C., "Turbulent jet Mixing at High Supersonic Speeds," *Zeitschrift Für Flugwissenschaften*, Vol. 21, No. 5, 1973, pp. 166–173.

[18]Schetz, J. A., Thomas, R. H., and Billig, F. S., "Mixing of Transverse Jets and Wall Jets in Supersonic Flow," *Separated Flows and Jets*, edited by V. V. Koslov and A. V. Dovgal, Springer-Verlag, Berlin, 1991, pp. 807–837.

[19]Cox, S. K., Fuller, R. P., and Schetz, J. A., "Vortical Interactions Generated by a Injector Array to Enhance Mixing in a Supersonic Flow," AIAA Paper 94-0708, Jan. 1994.

[20]Cox-Stouffer, S. K., and Gruber, M. R., "Effects of Spanwise Injector Spacing on Mixing Characteristics of Aerodynamic Ramp Injectors," AIAA Paper 98-3272, July 1998.

[21]Cox-Stouffer, S. K., and Gruber, M. R., "Effects of Injector Yaw on Mixing Characteristics of Aerodynamic Ramp Injectors," AIAA Paper 99-0086, Jan. 1999.

[22]Cox-Stouffer, S. K., and Gruber, M. R., "Further Investigations of the Effects of Aerodynamic Ramp Design Upon Mixing Characteristics," AIAA Paper 99-2238, July 1999.

[23]Fuller R. P., Wu, P.-K., Nejad, A. S., and Schetz, J. A., "Comparison of Physical and Aerodynamic Ramps as Fuel Injectors in Supersonic Flow," *Journal of Propulsion and Power*, Vol. 14, No. 2, 1998, pp. 135–145.

[24]Schetz, J. A., Cox-Stouffer, S. K., and Fuller, R. P., "Integrated CFD and Experimental Studies of Complex Injectors in Supersonic Flows (Invited)," AIAA Paper 98-2780, June 1998.

[25]Jacobsen, L. J., Schetz, J. A., and Ng, W. F., "Flowfield Near a Multiport Injector Array in a Supersonic Flow," *Journal of Propulsion and Power*, Vol. 16, No. 2, 2000, pp. 216–226.

[26]Eklund, D. R., and Gruber, M. R., "Study of a Supersonic Combustor Employing an Aerodynamic Ramp Pilot Injector," AIAA Paper 99-2249, June 1999.

[27]Gruber, M., Donbar, J., Jackson, T., Mathur, T., Eklund, D., and Billig, F., "Performance of an Aerodynamic Ramp Fuel Injector in a Scramjet Combustor," AIAA Paper 2000-3708, July 2000.

[28]"Assesment of Wind Tunnel Data Uncertainty," AIAA Paper S-071-1995, 1995.

[29]Crites, R. C., "Pressure Sensitive Paint Technique," *Measurement Techniques*, von Kármán Inst. for Fluid Dynamics, Lecture Series 1993-05, 1993.

[30]Tomioka, S., Jacobsen, L. S., and Schetz, J. A., "Modified Mixing Analogy for Studies of Mixing in Supersonic Flows," *Journal of Propulsion and Power*, Vol. 19, No. 1, 2003, pp. 151–153.

[31]Mao, M., Riggins, D. W., and McClinton C. R., "Numerical Simulation of Transverse Fuel Injection," NASP CR 1089, May 1990.